UC San Diego

UC San Diego Previously Published Works

Title

Non-uniform distribution of myosin-mediated forces governs red blood cell membrane curvature through tension modulation

Permalink

https://escholarship.org/uc/item/91p088x0

Journal

PLOS Computational Biology, 16(5)

ISSN

1553-734X

Authors

Alimohamadi, Haleh

Smith, Alyson S

Nowak, Roberta B

et al.

Publication Date

2020

DOI

10.1371/journal.pcbi.1007890

Copyright Information

This work is made available under the terms of a Creative Commons Attribution License, available at https://creativecommons.org/licenses/by/4.0/

Peer reviewed

eScholarship.org Powered by the California Digital Library
University of California

PLOS COMPUTATIONAL BIOLOGY

RESEARCH ARTICLE

Non-uniform distribution of myosin-mediated forces governs red blood cell membrane curvature through tension modulation

Haleh Alimohamadi[1], Alyson S. Smith[2], Roberta B. Nowak[2], Velia M. Fowler[2,3], Padmini Rangamani[1]*

1 Department of Mechanical and Aerospace Engineering, University of California San Diego, La Jolla, California, United States of America, **2** Department of Molecular Medicine, The Scripps Research Institute, La Jolla, California, United States of America, **3** Department of Biological Sciences, University of Delaware, Newark, Delaware, United States of America

* prangamani@ucsd.edu

Check for updates

OPEN ACCESS

Citation: Alimohamadi H, Smith AS, Nowak RB, Fowler VM, Rangamani P (2020) Non-uniform distribution of myosin-mediated forces governs red blood cell membrane curvature through tension modulation. PLoS Comput Biol 16(5): e1007890. https://doi.org/10.1371/journal.pcbi.1007890

Editor: Arne Elofsson, Stockholm University, SWEDEN

Received: November 26, 2019

Accepted: April 21, 2020

Published: May 26, 2020

Copyright: © 2020 Alimohamadi et al. This is an open access article distributed under the terms of the Creative Commons Attribution License, which permits unrestricted use, distribution, and reproduction in any medium, provided the original author and source are credited.

Data Availability Statement: All relevant data are within the paper and its Supporting Information files.

Funding: H.A. was supported by a fellowship from the Visible Molecular Cell Consortium (https://vmcc.ucsd.edu/). A.S.S. was supported by a fellowship from the NIH/National Center for Advancing Translational Sciences Clinical and Translational Science Award TL1 TR00113 (https://ncats.nih.gov/ctsa). V.M.F was supported by NIH grant HL083464 (https://www.nih.gov/grants-

Abstract

The biconcave disk shape of the mammalian red blood cell (RBC) is unique to the RBC and is vital for its circulatory function. Due to the absence of a transcellular cytoskeleton, RBC shape is determined by the membrane skeleton, a network of actin filaments cross-linked by spectrin and attached to membrane proteins. While the physical properties of a uniformly distributed actin network interacting with the lipid bilayer membrane have been assumed to control RBC shape, recent experiments reveal that RBC biconcave shape also depends on the contractile activity of nonmuscle myosin IIA (NMIIA) motor proteins. Here, we use the classical Helfrich-Canham model for the RBC membrane to test the role of heterogeneous force distributions along the membrane and mimic the contractile activity of sparsely distributed NMIIA filaments. By incorporating this additional contribution to the Helfrich-Canham energy, we find that the RBC biconcave shape depends on the ratio of forces per unit volume in the dimple and rim regions of the RBC. Experimental measurements of NMIIA densities at the dimple and rim validate our prediction that (a) membrane forces must be non-uniform along the RBC membrane and (b) the force density must be larger in the dimple than the rim to produce the observed membrane curvatures. Furthermore, we predict that RBC membrane tension and the orientation of the applied forces play important roles in regulating this force-shape landscape. Our findings of heterogeneous force distributions on the plasma membrane for RBC shape maintenance may also have implications for shape maintenance in different cell types.

Author summary

The spectrin-actin network of the membrane skeleton plays an important role in controlling specialized cell membrane morphology. In the paradigmatic red blood cell (RBC), where actin filaments are present exclusively in the membrane skeleton, recent experiments reveal that nonmuscle myosin IIA (NMIIA) motor contractility maintains the RBC

funding). P.R was supported by ONR N00014-17-1-2628 (https://www.onr.navy.mil/Contracts-Grants.aspx). The funders had no role in study design, data collection and analysis, decision to publish, or preparation of the manuscript.

Competing interests: The authors have declared that no competing interests exist.

biconcave disk shape. In this study, we have identified criteria for micron-scale distributions of NMIIA forces at the membrane required to maintain the biconcave disk shape of an RBC in the resting condition. Supported by experimental measurements of RBC NMIIA distribution, we showed that a heterogeneous force distribution with a larger force density at the dimple is able to capture the experimentally observed biconcave morphology of an RBC with better accuracy compared to previous models that did not consider the heterogeneity in the force distribution. Furthermore, we showed that the biconcave geometry of the RBC is closely regulated by the effective membrane tension and the direction of applied forces on the membrane. These findings can be generalized to any force-mediated membrane shape, providing insight into the role of actomyosin forces in prescribing and maintaining the morphology of different cell types.

Introduction

Cell shape and function are intricately coupled; cells must maintain specific shapes to migrate, divide normally, form tissues and organs during development, and support their physiological functions [1,2]. Maintenance or modification of cell shape is a concerted action of the actomyosin network at the whole cell level that allows for a stable actin network in polarized cells or a rapidly remodeling actin network for cell spreading and motility [3,4]. Thus, networks of actin filaments (F-actin) and the F-actin-activated motor protein non-muscle myosin II (NMII) specify cell shape by exerting forces on the plasma membrane to control membrane tension and curvature [5–8]. These actomyosin networks determine cell shapes and interactions during tissue morphogenesis in development [6,9–13] and their dysregulation has been implicated in cancer, [14–16], hearing disorders [17], podocyte filtration in the kidney [17,18], and neurodegeneration [19], among other physical issues. Local, nanoscale changes in actomyosin organization can lead to micron-scale changes in membrane curvature and cell shape to support normal cell function [20].

Human red blood cells (RBCs) have a biconcave disk shape, with a thin central dimple region surrounded by a thicker rim [21,22] (Fig 1). This shape enables efficient gas and ion exchange and increases RBC deformability and resilience in the circulation [23–25]. Due to its lack of transcellular cytoskeleton or internal organelles, RBC shape depends exclusively on the plasma membrane, and has long served as a simple model for membrane structure and function [26]. The RBC membrane is supported by the membrane skeleton, a two-dimensional network of short F-actins interconnected by long, flexible spectrin molecules [26,27], which bind to transmembrane proteins to maintain membrane tension, curvature, and mechanical properties of the RBC [23,24,26,28,29].

Historically, the biconcave disk shape of the RBC has been modeled as a thin elastic shell using the Helfrich-Canham energy model, treating the RBC as a lipid bilayer whose properties are spatially homogeneous along the entire RBC membrane [30,31]. This model, a classic in the field of membrane mechanics, was able to explain the observed RBC shape as a family of solutions for a given area and volume [30–32]. The calculated shapes corresponding to the minimal Helfrich-Canham local bending energy are scale invariant for zero spontaneous curvature [32]. Subsequent extensions of this model include consideration of reduced volume [30,31], spontaneous curvature [33], area differences between the two leaflets of the bilayer [34,35], and lateral distribution of membrane constituents [36–42]. A recent theoretical study predicted that the coupling between inhomogeneously distributed curved membrane protein inclusions and active cytoskeletal forces can govern the morphology of the membrane vesicles

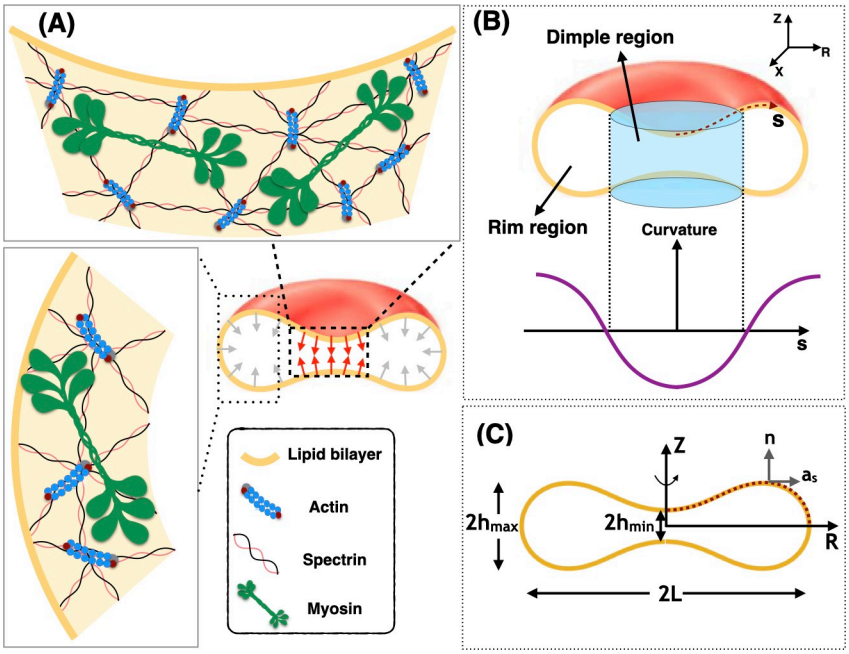

Fig 1. Schematic of membrane-myosin interactions in RBC. Interaction of the membrane and skeleton controls the shape of the RBC. (A) Schematic depiction of the biconcave disk shape of an RBC plasma membrane and the membrane skeleton underneath. The effect of NMIIA filaments (shown in green) is modeled by local forces applied to the plasma membrane (red and gray arrows). (B) Two distinct regions are identified in a biconcave RBC—the dimple and the rim regions. In the dimple region (blue cylinder), each RZ cross-section of the shape has a negative curvature along its arclength. In contrast, at the rim, the curvature of each RZ section is positive along the arclength. (C) The geometry of a simulated RBC in axisymmetric coordinates and the three characteristic length scales that represent the biconcave shape of the RBC. $2h_{min}$ is the minimum height at the dimple, $2h_{max}$ is the maximum height at the rim, and 2L denotes the cell's maximum diameter. The dotted red curve shows the computational domain for our mechanical model. **n** is the unit normal vector to the membrane surface and $\mathbf{a}_s$ is the unit tangent vector in the direction of arclength.

https://doi.org/10.1371/journal.pcbi.1007890.g001

[43,44]. Additional refinements have modeled the membrane as a two-component system composed of an incompressible lipid bilayer associated with an elastic spectrin-actin network uniformly distributed along the membrane [35,45–49].

To date, computational models to account for the biconcave disk shape of the RBC have not considered the contribution of actomyosin contractility even though RBCs contain NMII. NMIIA is the predominantly expressed isoform and has biochemical properties similar to NMIIs in other cell types [50–52]. Due to its low abundance, a potential role for NMIIA in RBC shape had been largely ignored by experimental biologists. However, we showed recently in Smith *et al.* [53] that RBC NMIIA forms bipolar filaments that bind to the membrane skeleton F-actin via their motor domains to control RBC membrane tension, biconcave disk shape and deformability [53] (Fig 1A). Specifically, we showed that blebbistatin inhibition of NMIIA motor activity in RBCs leads to loss of the biconcavity and the formation of elongated shapes, indicating an important role for NMIIA-generated forces in maintaining RBC biconcave disk shape and deformability [53]. Notably, the NMIIA filaments are sparsely distributed along the RBC membrane (~0.5 filaments per square micrometer), and thus would be expected to apply localized forces to the membrane [53]. However, it remains unclear how the magnitude and distribution of NMII-mediated localized forces could provide a mechanism to influence membrane curvature with respect to the morphology of RBCs.

In this study, motivated by our recent experimental observations [53], we investigated the role of local forces in modulating the shape of the RBC. We revisited the classical Helfrich-Canham model and modified it to account for localized forces representing the NMIIA-generated forces on the plasma membrane. By adding this extra degree of freedom to the classical Helfrich-Canham model, we sought to focus on how forces applied to the membrane, rather than spontaneous curvature or reduced volume, can result in the shapes that are comparable to the experimentally observed RBC shapes. To determine the set of force distributions that most closely reproduce experimentally observed RBC shapes, we varied the applied force heterogeneously along the membrane (Fig 1B).

Results

Model development

The RBC membrane is a thin elastic material that can bend but resists stretching. This feature enables the RBC to deform and adjust its shape in response to applied stresses. Here, we outline the assumptions underlying the development of the model and the associated governing equations of our model.

Assumptions

1. We consider that the radii of membrane curvatures are much larger than the thickness of the bilayer [33]. Therefore, we treat the lipid bilayer as a thin elastic shell and model the bending energy of the membrane using the Helfrich–Canham energy, which depends only on the local curvatures of the surface and compositional heterogeneities [30,31].
2. Due to the high stretching modulus of lipid bilayers, we assume that the membrane is locally incompressible [54]. We use a Lagrange multiplier to implement this constraint [55,56]. We refer the reader to [55,57] for a detailed interpretation of this Lagrange multiplier as membrane tension.
3. We assume that the RBC is at mechanical equilibrium at all times, allowing us to neglect inertia [58–60]. This assumption is consistent with the experimentally observed shapes for the resting RBCs in both *vivo* and *vitro* [61,62].
4. We assume that the total surface area of the RBC membrane is constant (~135 μm^2) [63,64].
5. For simplicity in the numerical simulations, we assume that the RBC is rotationally symmetric and also has a reflection symmetry with respect to the Z = 0 plane (see Fig 1C) [30,63,65,66]. This assumption reduces the computational cost of the simulation to simply calculating the shape of the curve shown by the red dotted line in Fig 1C.

Membrane mechanics

In mechanical equilibrium, the shape of the membrane in response to an applied force can be obtained as a result of the minimization of the membrane bending energy and the work done by the applied forces by the cytoskeleton. In this case, the total energy is given by [67,68]

$$\underbrace{E}_{\text{Total energy}} = \underbrace{E_b}_{\text{Bending energy}} - \underbrace{E_f}_{\text{Work done by forces}}, \quad (1)$$

where E is the total energy of the system, E_b is the bending energy and E_f is the work done by the applied forces given by

$$E_b = \int_\omega (W(H, K; \theta^\alpha) + \lambda(\theta^\alpha))da - pV, \tag{2A}$$

and

$$E_f = \int_\omega \mathbf{F}(\theta^\alpha).(\mathbf{r} - \mathbf{r_0})da. \tag{2B}$$

Here, ω is the total surface area of the membrane, W is the energy density per unit area, θ^α denotes the surface coordinate where $\alpha \in \{1,2\}$, H is the mean curvature, K is the Gaussian curvature, λ is the membrane tension (also see assumption 2), p is the pressure difference across the membrane, V is the enclosed volume, **F** is the force density per unit area representing the applied force density to the membrane surface by the NMIIA motor proteins, **r** is the position vector in the current configuration, and r_0 is the position vector in the reference configuration. The bending energy of the membrane is modeled using the Helfrich-Canham energy, defined by [30,31,55,57,69],

$$W(H, K; \theta^\alpha) = \kappa H(\theta^\alpha)^2 + \kappa_G K(\theta^\alpha) \tag{3}$$

where κ and κ_G are constants representing the bending and Gaussian moduli respectively [70]. To minimize the bending energy (Eq 1) and obtain the RBC shapes from simulations under the action of local forces, we used the variational approach which yields the so-called "shape equation" [57,71],

$$\underbrace{\kappa\Delta[H] + 2\,\kappa H(H^2 - K)}_{\text{Elastic effects}} = \underbrace{p + 2\,\lambda\,H}_{\text{Capillary effects}} + \underbrace{\mathbf{F}.\mathbf{n}}_{\substack{\text{Force due} \\ \text{to NMIIA}}}, \tag{4}$$

where Δ is the surface Laplacian (also known as the Laplace-Beltrami operator).

The incompressibility condition for the lipid membrane results in the spatial variation of membrane tension given by [57,71,72]

$$\underbrace{\lambda'}_{\substack{\text{Membrane tension} \\ \text{variation}}} = -\underbrace{\mathbf{F}.\mathbf{a_s}}_{\substack{\text{Force induced} \\ \text{variation}}}, \tag{5}$$

where $(.)'$ is the derivative with respect to the arclength. The shape equation (Eq 4) along with the incompressibility condition (Eq 5) represents the relationship between the forces applied by NMIIA motor proteins and the resulting shape of RBCs. A complete derivation of the governing equations of the force balance and the non-dimensionalization procedure are presented in S1 Text. All notations used in this manuscript are summarized in S1 Table and S2 Table. We refer the interested reader to [55,67] for details on the mathematical principles underlying these models.

Parameterization of RBC biconcave morphology and shape error estimation

The geometry of human RBCs has been studied extensively using a variety of different methods such as light microscopy [73,74], interference holography [75,76], resistive pulse spectroscopy [77], micropipette aspiration [78,79], and light scattering [80,81]. In Fig 2A, we summarize the reported values for the RBC geometrical parameters from the literature

(A)

Reference	2L (μm)	$2h_{min}$ (μm)	$2h_{max}$ (μm)	V (μm^3)	A (μm^2)	SI $(4.83(V)^{2/3}/A)$
Canham and Burton [73]	8.07 ± 0.55			107 ± 18.8	138 ± 17.4	0.783
Evans and Fung [75]	7.82 ± 0.62	0.81 ± 0.35	2.58 ± 0.27	94 ± 14	135 ± 17	0.742
Linderkamp et al. [78]	7.9 ± 0.4	1.84 ± 0.13		90.5 ± 4.4	137 ± 6.7	
Tarasov et al. [81]				87 ± 20	135 ± 28	
Ergul et al. [82]	7.7			80.9		
Das et al. [83]	9.52 ± 0.56					

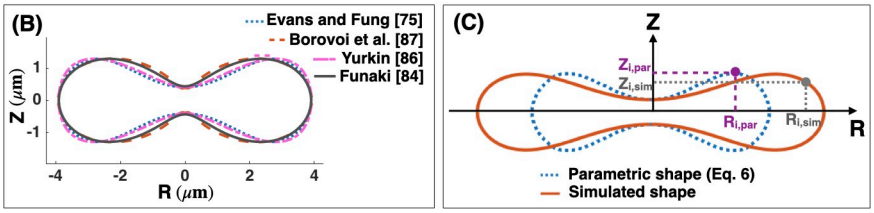

Fig 2. Parametric shape of a RBC. (A) Dimensions of healthy human RBC from the literature [73,75,78,81–83]. (B) Comparison between the proposed parametric models describing the biconcave morphology of an RBC. There is a close match between the four models for the fixed minimum height of the dimple, maximum height of the rim, and the maximum diameter (C) Discretization scheme of the parametric shape of an RBC (Eq 6) (dotted blue line) and the simulated geometry obtained from our mechanical model (Eqs 4 and 5) (solid red line). Each experimental and simulated shape is discretized into N nodes where i indicates the node index. These nodes are used to compute the total error in the simulated RBC geometry (Eq 8).

https://doi.org/10.1371/journal.pcbi.1007890.g002

[73,75,78,81–83] in terms of the three characteristic lengths (h_{min}, h_{max}, and L) (Fig 1C), the volume (V), the surface area (A), and the sphericity index (SI).

Several parametric models have been proposed to describe the biconcave morphology of the RBC [75,76,84–88]. Funaki proposed a Cassini oval model with two coefficients to represent the RBC geometry [84]. Kuchel et al. [85] and later Yurkin [86] modified the Cassini oval model to implicit equations with three and four coefficients, respectively. Borovoi *et al.* introduced a function in spherical coordinates to characterize the RBC morphology [87]. The most realistic model was proposed by Evans and Fung [75], where they first obtained images from 50 human RBC samples using light microscopy and then fitted a parametric equation to the RZ cross-sectional shape of the RBCs (Fig 1C) using statistical analysis. The function proposed by Evans and Fung is given by

$$Z(R) = \pm 0.5\sqrt{1-\left(\frac{2R}{L}\right)^2}\left(0.81 + 7.83\left(\frac{2R}{L}\right)^2 - 4.39\left(\frac{2R}{L}\right)^4\right), \quad (6)$$

where R is the radius from the axis of rotation and Z is the height from the base plane. In Fig 2B, we plotted the different proposed parametric models for the biconcave shape of an RBC. We observed that for the fixed height of the dimple (h_{min}), height of the rim (h_{max}), and the maximum diameter (L), all models generate similar shapes, but with slight differences. In this study, we used the Evans and Fung parametric equation in Eq 6 as the reference data for the experimental shape of an RBC, because Eq 6 was developed based on the direct experimental measurement and fit well with the observed RBC shapes [89,90].

To quantify the deviation between simulated geometries obtained from our mechanical model and the parametric shape equation for the RBC (Eq 6), we define three error metrics

—ϵ_{hmin}, ϵ_{hmax}, and ϵ_L as follows

$$\epsilon_{hmax} = \frac{|h_{max,par} - h_{max,sim}|}{L_{par}} = \frac{|\Delta h_{max}|}{L_{par}},$$

$$\epsilon_{hmin} = \frac{|h_{min,par} - h_{min,sim}|}{L_{par}} = \frac{|\Delta h_{min}|}{L_{par}}, \tag{7}$$

and

$$\epsilon_L = \frac{|L_{par} - L_{sim}|}{L_{par}} = \frac{|\Delta L|}{L_{par}},$$

where $(.)_{,par}$ is the experimentally measured length scale fitted to the parametric equations (Eq 6) and $(.)_{,sim}$ is the length scale obtained from the numerical simulation (Eqs 4 and 5). The total error (ϵ_{total}) in the shape of the simulated RBCs is then calculated by the root mean square between every two mapped points in the parametric shape of an RBC and the simulated geometries (Fig 2C) given by

$$\epsilon_{total} = \frac{\sqrt{\frac{1}{N}\left[\sum_{i=1}^{i=N}(Z_{i,sim} - Z_{i,par})^2 + (R_{i,sim} - R_{i,par})^2\right]}}{L_{par}}, \tag{8}$$

where N is the total number of nodes across the RBC shapes, i is the index node, $Z_{i,sim}$ and $Z_{i,par}$ are the height of the simulated and the parametric (Eq 6) RBC shape at index i, respectively. $R_{i,sim}$ is the radius of the simulated shape at index i, and $R_{i,par}$ is the radius of the RBC parametric shape (Eq 6) at index i.

While Eq 8 represents the error in the simulated shapes compared to the RBC parametric shape, it does not capture measurement errors as Eq 6 was developed based on the average dimensions of experimentally observed RBCs. However, there are standard deviations in the measured dimensions as reported by Evans and Fung [75] and the resolution of imaging methods introduces additional uncertainties. Here, to account for these uncertainties, we assume that the given parametric equation by Evans and Fung [75] can be written as

$$Z(R) = Z_{mean}(R) + Z_{error}(R), \tag{9}$$

where $Z_{mean}(R)$ is the given function in Eq 6 and we define $Z_{error}(R)$ as the fitting error of the Evans and Fung parametric equation to the actual shape of an RBC. In this study, we assume that $Z_{error}(R)$ is approximately 10% of $Z_{mean}(R)$ in order to represent the variance of RBC dimensions.

Numerical simulation

Simplifying the shape equation (Eqs 4 and 5) for a rotationally symmetric RBC gives us a set of first order differential equations (Eq. S11 in S1 Text). In order to obtain the RBC shapes from simulations and determine the role of NMIIA-generated forces in maintaining the biconcave morphology, we need to solve the coupled differential equations (Eq. S11 in S1 Text) for the defined boundary conditions (Eq. S12 in S1 Text). Here, we used the commercially available finite element solver COMSOL MULTIPHYSICS 5.3a to solve the governing differential equations (Eqs. S11 and S12 in S1 Text). In all our simulations, the transmembrane pressure is set to zero (p = 0).

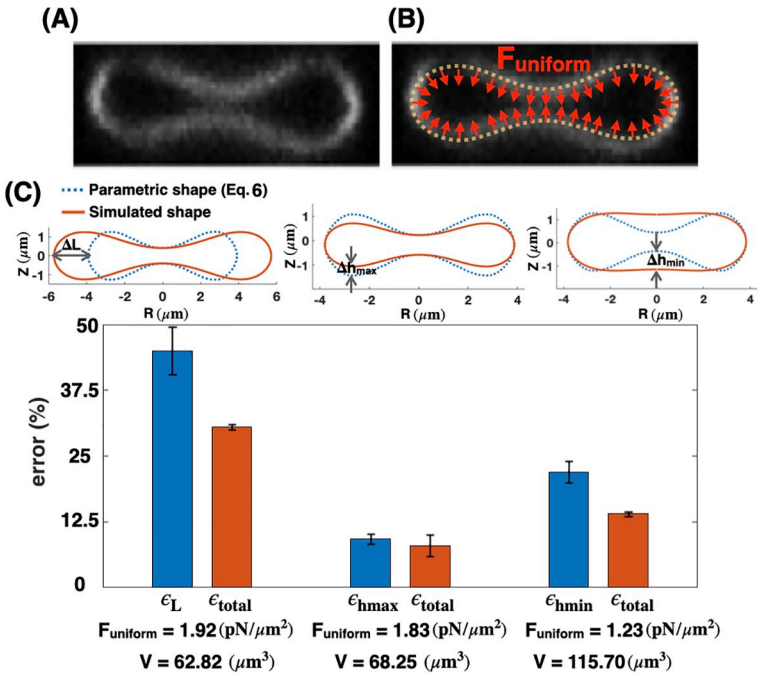

Fig 3. Uniform force distribution. Mismatch between the parametric shape of an experimentally observed RBC (Eq 6) and the shapes obtained from simulations (Eqs. S10 in S1 Text) with a uniform distribution of the pulling force density across the membrane surface. (A) RZ view of the center of an RBC from a confocal Z-stack of an RBC stained for the membrane marker glycophorin A. (B) Schematic of a biconcave RBC with a uniform distribution of the normal pulling force density (red arrows). $F_{uniform}$ represents the magnitude of the pulling force density. (C) Calculated error in the characteristic length scales (Eq 7), and total shape error (Eq 8) for different values of the force density. The total shape error (ϵ_{total}) calculated by Eq 8 is minimum for $F_{uniform}$ = 1.83 pN/μm^2, when there is only a mismatch in the maximum height of the RBC morphology (center bar). For all three values of the applied uniform force densities, the calculated volume (V) is shown on the X-axis and is significantly different from the reported experimental data.

https://doi.org/10.1371/journal.pcbi.1007890.g003

Uniform distribution of force density across the membrane surface is not sufficient to recover the biconcave shape of an RBC

Modeling studies of RBC shapes have been based on the assumption that the RBC membrane and skeleton are spatially homogeneous [23,24,26,70]. Therefore, we first performed simulations with a uniform pulling force density ($F_{uniform}$) applied normally on the membrane surface (Fig 3A and 3B). This uniform pulling force density can be interpreted as a pressure difference between the inside and outside of the RBC that specifies the change in the RBC volume compared to an equivalent sphere (the reduced volume) [32,33,91].

To perform our simulations, we assumed that the RBC membrane area is large enough that the lateral membrane tension is negligible ($\lambda = 0$) [92–94]. We also set the bending modulus to be in the range of physiologically reported values for the RBC membrane ($\kappa = 9 \times 10^{-19}$ J) [93]. For a given value of uniform pulling force, we were able to match two out of three characteristic length scales of the simulated shapes with the parametric shape of an experimentally observed RBC (Eq 6) (see Fig 3B). Furthermore, we observed that for all configurations in Fig 3C, the calculated uniform force density from our mechanical model is in the order of the reported pressure difference for a biconcave RBC ($F_{uniform} \sim O(1)$ pN/μm^2), which validates our numerical results (Fig 3C, bottom row).

We observed that for the large value of the pulling force density ($F_{uniform}$ = 1.92 pN/μm^2), the maximum and the minimum heights of the simulated shape match well with the parametric shape, while the maximum diameter does not (Fig 3C, left). For the intermediate pulling

force density ($F_{uniform}$ = 1.83 pN/μm^2), the minimum height and the maximum diameter of the simulated shape are in good agreement with the parametric shape, but the maximum height is not (Fig 3C center). Finally, for the small pulling force density ($F_{uniform}$ = 1.23 pN/μm^2), the mismatch between the simulated geometry and the parametric shape of the RBC is in the minimum height of the dimple (Fig 3C right). For each value of the applied pulling force density, we calculated the error for each of the characteristic lengths (L, h_{max} or h_{min}) (Eq 7) and the total error (Eq 8) (Fig 3C). We found that both characteristic and the total shape errors have the lowest value (ϵ_{hmax}~ 10.23% and ϵ_{total} ~ 8.2%) at the intermediate uniform force density and there is only a relatively small mismatch in the maximum height (Δh_{max}) (Fig 3C center). Thus, we can predict that among the three main characteristic length scales of an RBC, the maximum height of the rim (2) appears to be the least critical dimension in order to minimize the shape error of the simulated geometries. It should be mentioned that for each case here, we first calculated the mean errors based on the given parametric equation (Eq 6) and then we computed the error bars using Eq 9.

In addition to the biconcave shape of an RBC, the volume of the RBC is one of the critical parameters that is regulated by multiple transport systems [91]. We calculated the volume of each simulated geometry (V) using Eq. S13b in S1 Text (Fig 3C). We found that for all three values of the uniform force densities, the volume of the simulated shapes is far from the reported experimental data in Fig 2A. For the large and the intermediate force densities ($F_{uniform}$ = 1.92 pN/μm^2 and $F_{uniform}$ = 1.83 pN/μm^2), the volumes of the simulated geometries (Fig 3C) are much smaller than the reported values, which range from V = 80 μm^3 to V = 107 μm^3 given in Fig 2A. In contrast, for the small force density ($F_{uniform}$ = 1.23 pN/μm^2), the volume of the shape obtained from the simulation is significantly larger than the experimental values (Fig 3C).

Local force density at the RBC dimple reduces the shape error

Given that the shape mismatch and volume difference of the simulated RBC (Fig 2) are relatively large compared to the experimentally measured RBC dimensions, we next asked if we could change the distribution of the non-uniform pulling force density to reduce the shape error and obtain a better agreement between the experimentally reported shapes for RBCs and our model. We conducted simulations of Eqs S11, S12 in S1 Text but now assumed that the applied normal force per unit area is locally concentrated in the dimple region (F_{dimple}) and that there is no force along the surface of the rim (Fig 4A and 4B). This heterogeneous force distribution along the membrane was implemented using a hyperbolic tangent function (Eq. S24 in S1 Text).

In Fig 4C, we compare the RBC shapes obtained from the simulation with the application of increased local pulling force density at the dimple. We found that the total error is a nonmonotonic function of F_{dimple}; as F_{dimple} increases, the total error in shape mismatch decreases and then increases again. Based on the shape of the simulated RBC, we can identify three different regimes (Fig 4C). For low dimple force density (F_{dimple}< 1.81 pN/μm^2), the simulated geometry has a spherical shape (h_{max} = h_{min}) and therefore the shape error is large (ϵ_{total} > 50%) (yellow area in Fig 4C). With increasing the magnitude of dimple force density (1.81 pN/μm^2 < F_{dimple}< 3.73 pN/μm^2), the dimple forms biconcave shapes where h_{max} > h_m and the shape error decreases sharply (purple area in Fig 4C). When higher levels of force are applied at the dimple (F_{dimple}> 3.73 pN/μm^2), the error increases because the distance between the two bilayers in the dimple becomes too narrow (kissing shapes where h_{min} = 0) (Fig 4C). We also observed a similar nonmonotonic trend in the calculated errors for the characteristic lengths (Eq 7) as a function of dimple force density (S1 Fig).

Based on our results in Fig 4C, the shape error has a minimum value of ϵ_{total} ~ 5.62% for the case where F_{dimple} = 3.73 pN/μm^2. This total error is less than that for all the simulated shapes

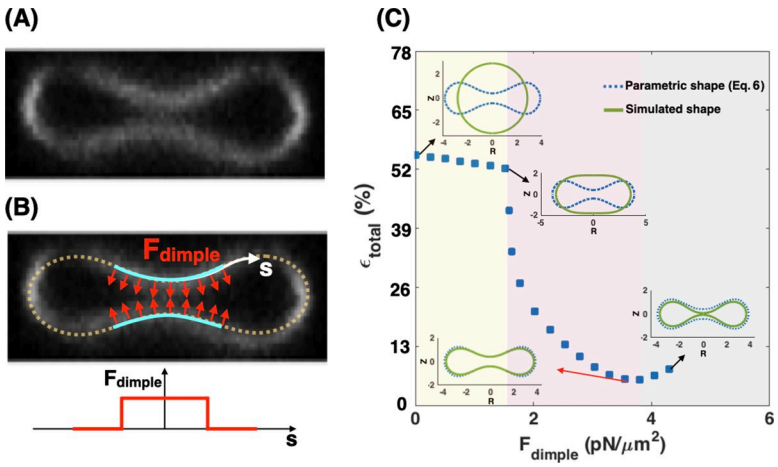

Fig 4. Local force density at the RBC dimple. A local distribution of the pulling force density at the RBC dimple results in a better agreement between the parametric shape of an RBC (Eq 6) and the shape obtained from the simulation. (A) RZ view of the center of an RBC from a confocal Z-stack of an RBC stained for the membrane marker glycophorin A. (B, upper) A schematic depicting a biconcave RBC with a local force at the dimple area (red arrows) and no force in the rim region. F_{dimple} represents the magnitude of the pulling force density in the dimple region. (B, lower) The applied force density at the dimple as a function of the arclength (Eq. S24 in S1 Text). (C) The simulated shape of the RBC with a local pulling force density in the dimple (solid green line) in comparison with the RBC parametric shape (dotted blue line). (C) The nonmonotonic behavior of the total error when increasing the dimple force density (F_{dimple}). Three different regimes can be identified based on the shape of the simulated RBC; *(i)* the spherical shapes where $h_{max} = h_{min}$ for the low F_{dimple} (yellow area), *(ii)* the biconcave shapes where the dimple forms ($h_{max} > h_{min}$) for the mid-range of F_{dimple} (purple area), and *(iii)* the kissing shapes where $h_{min} \rightarrow 0$ for large F_{dimple} (gray area). The shape error has the lowest value at $F_{dimple} = 3.73$ pN/μm^2 ($\epsilon_{total} \sim 5.62\%$) when the minimum height of the dimple in the simulated geometry matches closely with the minimum height of the parametric shape. The volume of the simulated RBC at $F_{dimple} = 3.73$ pN/μm^2 is about 76.78 μm^3.

https://doi.org/10.1371/journal.pcbi.1007890.g004

determined in the case of a uniform force applied to the membrane (Fig 3C). We found that the volume of the simulated RBC at $F_{dimple} = 3.73$ pN/μm^2 is about V = 76.78 μm^3, which is closer to the reported experimental value for the RBC volume by Evans and Fung [75]. From these results, we can conclude that there is a better agreement between the simulated shape and the parametric shape of an experimentally observed RBC when a localized force is applied at the RBC dimple compared to the case with a uniform force distribution (Fig 3).

Non-uniform distribution of force density in the RBC dimple region versus the rim region minimizes the shape error

While localizing the force density at the dimple decreased the error and the volume mismatch in our simulated RBC shapes, NMIIA is known to be distributed throughout the RBC [53]. Therefore, we next asked if the shape error can be minimized by including a normal force at the rim region in addition to the applied force at the dimple region (Fig 5A). This analysis allowed us to predict the RBC shape not only in terms of absolute values of forces in the dimple and rim regions but also as a function of force per unit volume ratio in these two regions. In our model, based on the given force density per unit area in the dimple (Fdimple) and rim (Frim) regions, we defined the ratio of forces per unit volume as

$$F_{ratio} = \frac{F_{dimple}}{F_{rim}} \times \frac{A_{dimple} V_{rim}}{A_{rim} V_{dimple}}, \quad (10)$$

where A_{dimple} and A_{rim} are the area of the membrane surface in the dimple and rim regions, and V_{dimple} and V_{rim} are the volume occupied by the dimple and rim regions, respectively. For

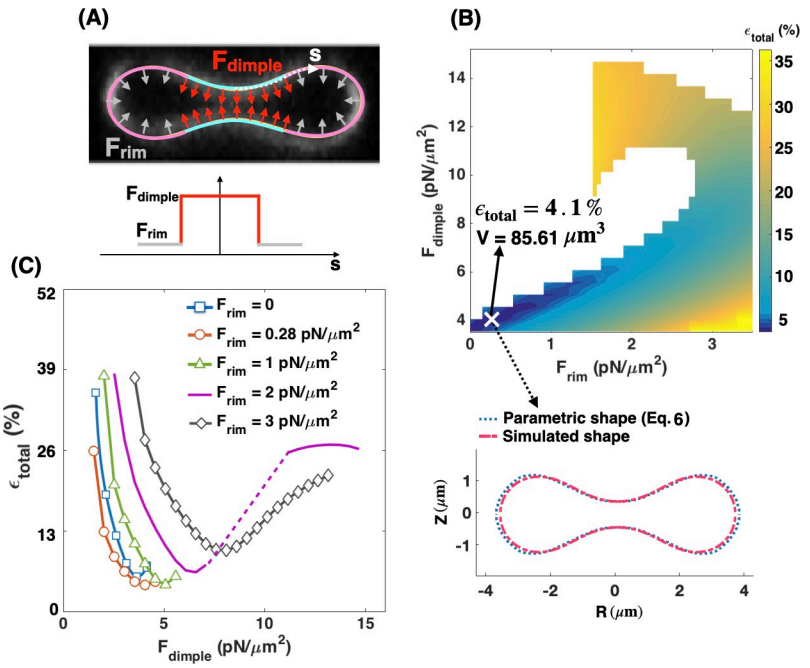

Fig 5. Heterogeneous forces in the RBC dimple and rim. The applied force densities at the RBC dimple and rim regions regulate the shape error. (A, upper) Schematic of a biconcave RBC with a large force density (red arrows) at the dimple and a small force density (gray arrows) at the rim region. Schematic is overlaid on an RZ view of the center of an RBC from a confocal Z-stack of an RBC stained for the membrane marker glycophorin A. (A, lower) The applied force density along the membrane as a function of the arclength (Eq. S24 in S1 Text). (B) Heat map shows the calculated shape error (Eq 8) for a range of the force densities at the dimple (F_{dimple}) and rim (F_{rim}) regions. We stopped the simulations when the height at the dimple tends to zero ($h_{min} \rightarrow 0$). The marked point **X** shows the case that has the lowest value of the error in the heat map at F_{dimple} = 4.05 pN/μm^2 and F_{rim} = 0.28 pN/μm^2 (ϵ_{total} ~ 4.1%) with V = 85.61 μm^3. A comparison between the parametric shape of an RBC (dotted blue line) and the shape obtained from the simulation at point **X** (dashed red line) is shown in the lower panel. (C) The shape error as a function of force density at the dimple (F_{dimple}) for five different values of the applied force density at the rim region. The dotted purple line shows a discontinuous transition in the shape error with increasing the dimple force density for F_{rim} = 2 pN/μm^2. Similar to Fig 4B, independent of the value of F_{rim}, the total error is a nonmonotonic function of the dimple force density (F_{dimple}).

https://doi.org/10.1371/journal.pcbi.1007890.g005

a given RBC shape, the area and the volume of the dimple and rim regions can be calculated by Eq. S13a and Eq. S13b in S1 Text, respectively.

We begin our analysis with the case where the pulling force in the dimple area is larger than the pulling force in the rim area ($F_{rim} < F_{dimple}$). We implemented this distribution of force along the RBC membrane using a hyperbolic tangent function (Eq. S24 in S1 Text) and performed the simulations over a range of forces at the dimple and the rim regions (F_{dimple} = 3.5–14 pN/μm^2 and F_{rim} = 0–3.5 pN/μm^2). The range of dimple force (F_{dimple}) was chosen based on our previous results (Fig 4) to have a close comparison with the parametric shape and obtain biconcave shapes from simulations with $h_{max} > h_{min}$ and $h_{min} > 0$. The force along the rim (F_{rim}) was set between F_{rim} = 0 and F_{rim} = 3.5 pN/μm^2 based on the imposed condition of $F_{ratio} < 1$ for all simulations.

The heat map in Fig 5B represents the magnitude of the shape error for a given force density at the dimple and rim area. The simulations were stopped when the height at the RBC dimple approached zero, shown as white domains in the heat map (Fig 5B). Based on these calculations, we found that the shape error has the lowest value (ϵ_{total} ~ 4.1%) when F_{dimple} = 4.05 pN/μm^2 and F_{rim} = 0.28 pN/μm^2 (the point **X** on the heat map). For these specific force values, the parametric shape of the RBC (Eq 6) and the shape obtained from the simulation at point **X**

were very well-matched (Fig 5B lower panel). Additionally, the volume of the simulated shape at point (**X**), is close (V = 85.62 μm^3) to the experimentally reported value by Evans and Fung [75].

To further understand the relationships between F_{rim} and F_{dimple} in governing the shape of the RBC, we plotted the shape error as a function of F_{dimple} for five different values of the force density at the rim section (Fig 5C). We found that the shape error shows the same nonmonotonic dependence for different values of F_{rim}. By increasing the value of F_{dimple}, the shape error initially decreases by an order of magnitude and attains a relative minimum for each curve (Fig 5C). Any further increase in the dimple force density results in a larger shape error (Fig 5C), similar to Fig 4B. As expected from Fig 5B, the shape error has the lowest value on the red curve (F_{rim} = 0.28 pN/μm^2) when F_{dimple} = 4.05 pN/μm^2. Using Eq 10, this set of dimple and rim forces in Fig 5B is equivalent to F_{ratio}~ 14.27, which reflects the fact that to obtain the best match between the simulated RBC shape and the experimentally observed morphology, 14.27 times larger force per unit volume should be applied in the dimple region than the rim region.

Thus far, we have only considered the cases in which NMIIA motors were able to exert small pulling forces in the rim region. However, two other force configurations are possible: *(i)* NMIIA motors apply a larger force density in the rim region than the dimple area ($F_{rim} > F_{dimple}$) (panel A in S2 Fig), and *(ii)* NMIIA motors exert pushing forces in the rim region (panel A in S3 Fig). We found that a large pulling force in the rim region ($F_{rim} > F_{dimple}$) generates a shape resembling a peanut-shaped vesicle with a large shape error of $\epsilon_{total} >> 50\%$ (S2 Fig). We also observed that applying a pushing force in the rim region (F_{rim} = 3.73 pN/μm^2) with no force in the dimple causes an error of ϵ_{total} ~ 12.5% (panel B in S3 Fig). Even adding a small pushing force in the rim region (F_{rim} = 0.53 pN/μm^2) with F_{dimple} = 3.73 pN/μm^2 increases the shape error to ϵ_{total} ~ 9.7% (panel C in S3 Fig). Our major prediction is that RBC biconcave shape depends on a heterogeneous distribution of NMIIA forces, which can be accomplished by more NMIIA motors density in the dimple compared to the rim.

RBC dimple region has a higher concentration of the NMIIA puncta as compared to the rim region

Our simulations suggest that NMIIA-mediated force densities are not uniformly distributed across the RBC membrane but instead are larger in the dimple region than the rim region (Fig 5). Therefore, we hypothesized that the NMIIA distribution in RBCs is also non-uniform, with more NMIIA in the dimple region than the rim region. To test this hypothesis, we localized NMIIA motor domain puncta in three-dimensional reconstructions of AiryScan confocal Z-stacks [53,95] (Fig 6A). The puncta in these images are individual NMIIA bipolar filaments, based on our previous study showing that that RBCs contain ~150 NMIIA puncta/cell [53], consistent with calculations of numbers of NMIIA bipolar filaments/cell using quantitative biochemical assays [50].

We divided each RBC into dimple and rim regions based on F-actin staining at the membrane (Fig 6B) and quantified the number of NMIIA motor domain puncta in each region and the volumes of each region and the whole RBC using Volocity software. The dimple region accounted for about 7.4% of the total RBC volume (based on the F-actin staining, Fig 6C). This value agrees with calculations of dimple volume (~7.1% of total volume) from our simulated shapes, in which we classify the dimple and rim regions based on the sign of the local mean curvature (Fig 1B). The number of NMIIA puncta varies between RBCs, with 125 ± 47 puncta in the whole RBC, 113 ± 42 puncta in the rim, and 12 ± 9 puncta in the dimple (all values are mean ± SD). The dimple region contains about 9.1% of the total NMIIA motor domain puncta (Fig 6D). In the dimple and rim regions as well as the whole RBC, the number of NMIIA puncta tends to increase with increasing the region or cell volume (S4 Fig).

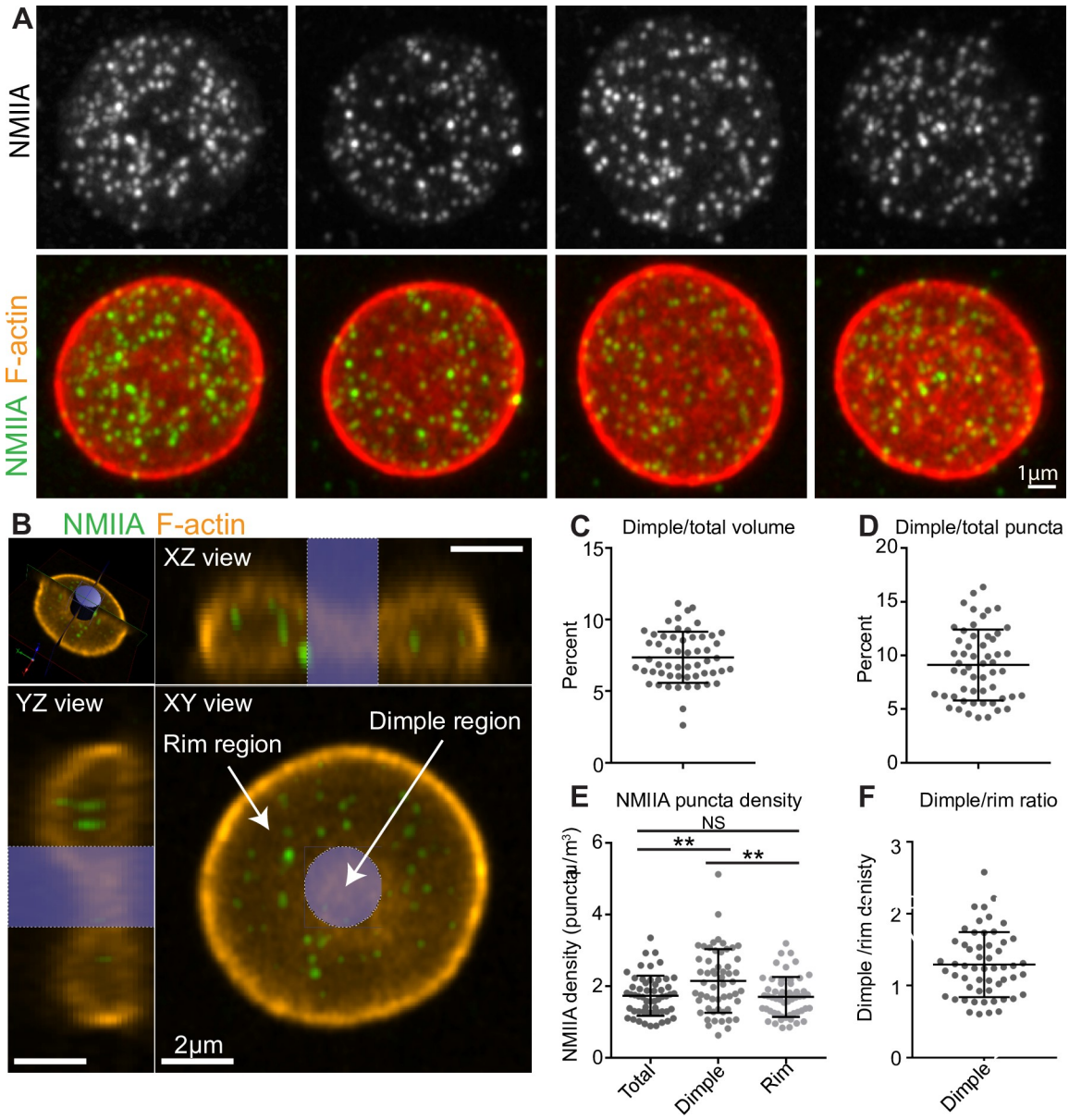

Fig 6. Experimental measurement of NMII puncta. The RBC dimple has a higher average NMIIA puncta density than the RBC rim. (A) Maximum intensity projections of super-resolution Airyscan confocal Z stacks of individual human RBCs immunostained with an antibody to NMIIA motor domain (grey scale, top row), together with merged images (second row) of NMIIA (green) and rhodamine phalloidin for F-actin (red). (B) Schematic illustrating volume segmentation of RBCs and NMIIA puncta distribution. Optical section of a super-resolution Airyscan confocal Z-stack of human RBC immunostained with an antibody to the motor domain of NMIIA (green) and rhodamine-phalloidin for F-actin (orange). The top left image shows a perspective view of the optical section. Top right and bottom left images show YZ and XZ slices, respectively, of the RBC from planes perpendicular to this optical section. The bottom right image shows an XY view of the optical section. The blue cylinder represents the region identified as the dimple region. The rest of the RBC is identified as the rim region. Note, the myosin puncta near the RBC membrane are difficult to visualize in these merged images due to the bright F-actin staining. (C) The percent of total RBC volume occupied by the dimple region. Mean ± S.D. = 7.37 ± 1.79. (D) The percent of total NMIIA puncta in the dimple region. Mean ± S.D. = 9.11 ± 3.30. (E) The RBC dimple region has a ~25% higher density of NMIIA puncta than whole RBCs (Total) ($p = 0.0051$) or the rim region ($p = 0.0023$) by Tukey's multiple comparisons test. Mean ± S.D.: Total = 1.73 ± 0.562; Dimple = 2.15 ± 0.888; Rim = 1.70 ± 0.556. (F) Ratio of dimple and rim region NMIIA puncta densities for each RBC. Mean ± S.D. = 1.29 ± 0.452. (C-F) n = 55 RBCs from 3 individual donors.

https://doi.org/10.1371/journal.pcbi.1007890.g006

The number of NMIIA puncta per unit volume (μm^3) in an RBC region is likely proportional to the number of NMIIA filaments that interact with membrane skeleton F-actin to exert force on the RBC membrane. The whole RBC and the rim region have similar NMIIA puncta densities (1.73 ± 0.562 μm^3 and 1.70 ± 0.556 μm^3, respectively), while the dimple region has a ~25% higher density (2.15 ± 0.888 μm^3) (Fig 6E). Thus, the dimple region has ~1.29 times higher NMIIA puncta density compared to the rim region (Fig 6F).

To determine whether differences in NMIIA densities relate to the extent of RBC biconcavity, we related NMIIA density to the minimum and maximum heights of XZ slices at the center of each RBC (S5 Fig). In both whole RBCs (panel A in S5 Fig) and the dimple region (panel C in S5 Fig), RBC biconcavity increased with increasing NMIIA density, while NMIIA density in the rim region was not related to biconcavity (panel B in Fig). These results agree with the results of our simulations, which predict that the maximum height of the rim (h_{max}) is the least critical dimension to minimize the shape error (Fig 3) and furthermore, that NMIIA exerts a larger force density at the RBC dimple (Fig 5). Together, our simulations and experimental data suggest that this non-uniform force distribution is required to specify RBC biconcave disk shape.

Effective membrane tension regulates the required force densities ratio in the RBC dimple versus the rim region

We found that for the simulated RBC shapes, the shape error is minimized when the force per unit volume applied normally in the dimple region is about 14.27 times larger than the force per unit volume applied in the rim region (F_{ratio} = 14.27), in a tensionless membrane (Fig 5). However, our experimental measurements reveal that in a healthy human RBC, the dimple region has only ~25% higher density of NMIIA puncta than the rim region (Fig 6). If we assume that the NMIIA density is proportional to the force generation capacity, then the induced force in the dimple region should be 1.25 times larger than the rim area. Therefore, we set out to reconcile the predicted F_{ratio} and measured the NMIIA density ratio. Literature suggests that the membrane tension in RBCs can vary from 10^{-1} pN/nm to 10^{-4} pN/nm [70,93,96]. Here, we interpret membrane tension to be the effective contribution of the membrane in-plane stresses and the membrane-cytoskeleton interactions [97]. We hypothesized that this in-plane tension of the RBC could play a critical role in relating the RBC shape to the NMIIA-generated force ratio in dimple and rim regions.

To investigate how this variation in membrane tension can modulate F_{ratio} and the shape error, we repeated the simulations as in Fig 5 for three different effective membrane tensions: *(i)* low membrane tension (tension = 10^{-4} pN/nm) (Fig 7A), *(ii)* intermediate membrane tension (tension = 10^{-3} pN/nm) (Fig 7B), and *(iii)* high membrane tension (tension = 10^{-2} pN/nm) (Fig 7C). The marker (**X**) in each heat map shows the point with minimum shape error for that set of simulations. To visualize the geometry of the simulated RBC at each point marked with an '**X**', we plot the shapes that were obtained from simulations (solid yellow line) versus the reference experimental data (dotted blue line) [75] and also calculated the volume of the simulated geometry using Eq. S13b in S1 Text.

We observe that the shape error remains almost constant (ϵ_{total} ~3.8%) with increasing the membrane tension from zero to low and intermediate values (Fig 7A and 7B). However, varying the membrane tension alters the force ratio that gives the minimum shape error as well as the volume of the simulated geometry. For example, at low tension, the minimum shape error occurs at F_{ratio} = 4.35 where V = 79.62 μm^3 and at intermediate tension the shape error is minimum when F_{ratio} = 1.27 with V = 91.37 μm^3 (Fig 7A and 7B), close to the volume experimentally reported by Evans and Fung [75]. In the case of high membrane tension, we found that

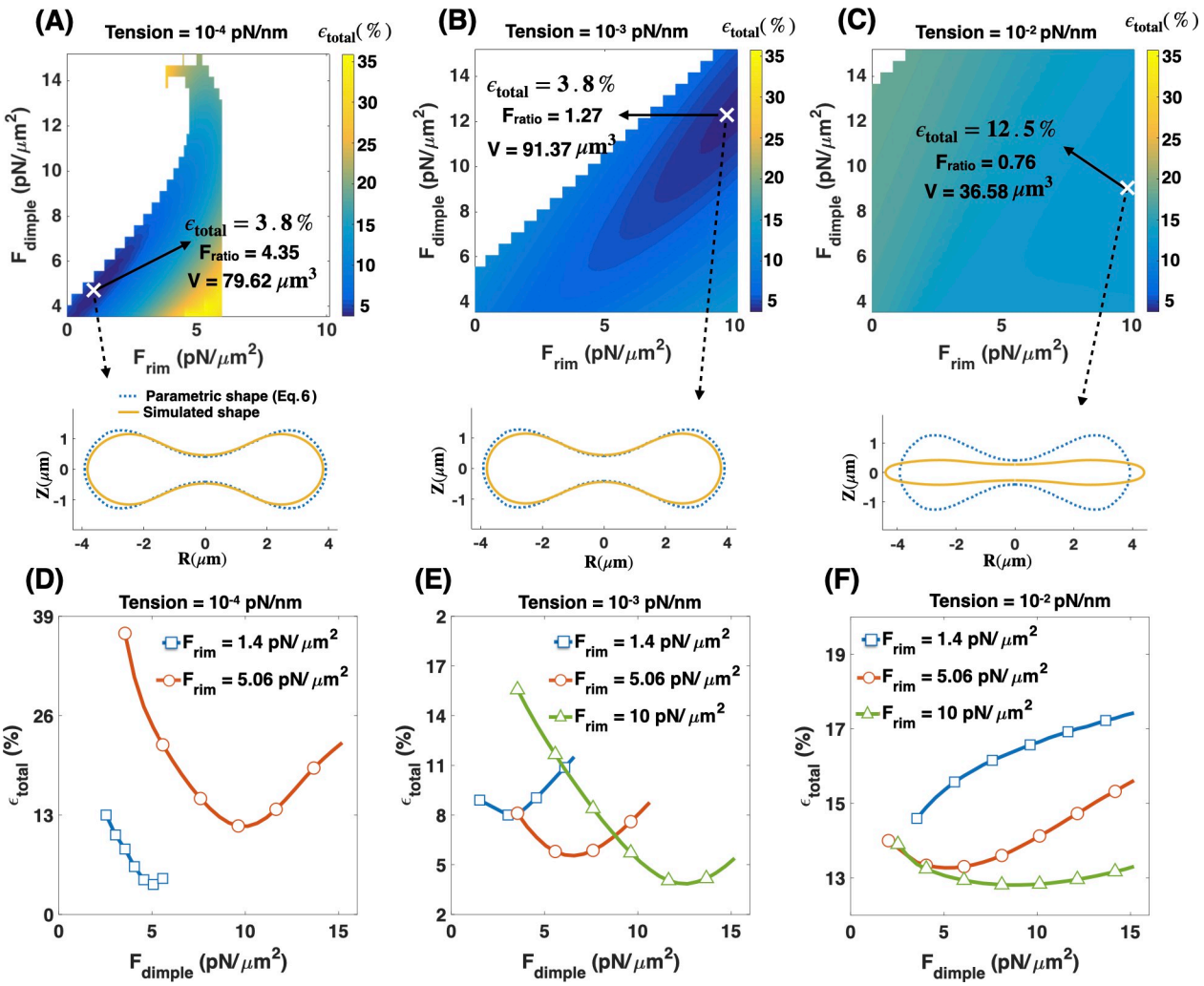

Fig 7. The role of effective tension. Effective membrane tension is a key parameter in regulating the RBC biconcave shape in addition to applied forces in the dimple and rim regions. (A-C) Heat maps show the total error in the shape of the simulated RBCs for (A) low tension (tension = 10^{-4} pN/nm), (B) intermediate tension (tension = 10^{-3} pN/nm), and (C) high tension (tension = 10^{-2} pN/nm). In each heat map, the point with the minimum error is marked with **X**. Also, for each marked point, the volume of the simulated RBC (V) is calculated using Eq. S13b in S1 Text, and the shape (solid yellow line) is shown in comparison with the reference parametric shape (dotted blue line). At intermediate tension, the shape error has the lowest value when F_{ratio} = 1.27 consistent with our experimental results in Fig 6. (D-F) The calculated shape error (Eq 8) as a function of the dimple force density (F_{dimple}) for different values of the force density at the rim region and the membrane tension.

https://doi.org/10.1371/journal.pcbi.1007890.g007

the simulated shape deviates significantly from the biconcave disk and becomes closer to a pancake with a small volume (V = 36.58 μm^3) and the error goes up noticeably to about 12 percent (ϵ_{total} ~ 12.5%) (Fig 7C).

Additionally, we found that for low and intermediate tensions independent of the value of F_{rim}, the shape error has the same non-linear relationship with increasing F_{dimple} as previously observed for the tensionless membrane (Fig 7D and 7E). At low tension, the minimum shape error occurs when F_{dimple} = 5.06 pN/μm^2 and F_{rim} = 1.4 pN/μm^2 (blue square line) (Fig 7D). At intermediate tension, a combination of F_{dimple} = 12.66 pN/μm^2 and F_{rim} = 9.95 pN/μm^2 gives the minimum shape error (green triangle line) (Fig 7E). However, for high tension, because of the stiffness of the membrane, we observe not only a deviation from the biconcave shape but also a deviation from the nonmonotonic error—dimple force relationships (Fig 7F).

Based on these results, we concluded that in addition to a non-uniform force distribution along the RBC membrane, a non-zero intermediate tension is required to obtain a close match between the shape and the volume of the simulated RBC and the experimental data. Furthermore, the intermediate value of tension (tension = 10^{-3} pN/nm) gives an excellent quantitative match for the predicted value of F_{ratio} (Fig 7B) and the experimentally observed NMIIA density ratio (Fig 6).

The angle of applied forces in the RBC dimple and rim regions controls the shape error

Until now, we have assumed the net effects of NMIIA motor proteins act as local forces applied normally to the membrane surface. However, there is evidence that these molecules also exert forces tangential to the membrane [98]. To examine how the orientation of the induced forces by NMIIA can affect the morphology of the RBC, we repeated the simulation in Fig 7 for different membrane tension values assuming that the applied forces make an angle ϕ with the tangent vector $\mathbf{a_s}$ (Fig 8A). Because the exact orientation of the applied forces by NMII molecules is currently unknown, we varied angle ϕ from $\phi = 90^0$ (normal to the membrane) to $\phi = 0$ (tangential to the membrane) and for each case found the combination of the force densities that gives the minimum shape error (S6 Fig, S7 Fig, S8 Fig and S9 Fig).

In Fig 8B–8D, we plotted the minimum shape error as a function of angle ϕ for three different values of the membrane tension; (B) tensionless membrane, (C) low membrane tension (tension = 10^{-4} pN/nm), and (D) intermediate tension (tension = 10^{-3} pN/nm). We observed that in all three cases, with varying the angle ϕ from normal to tangential orientation, the simulated shapes deviate from the biconcave disks to the pancake shapes with an almost three times larger shape error. Based on our results, we found that for tensionless membranes, the transition from the biconcave shapes with $\epsilon_{total} < 5\%$ (pink area) to the pancake shapes where $\epsilon_{total} >> 5\%$ (gray area) occurs for angles smaller than 45^0 ($\phi < 45^0$) (Fig 8B). This transition to pancake shapes shifted toward the smaller angles ($\phi < 30^0$) for low and intermediate

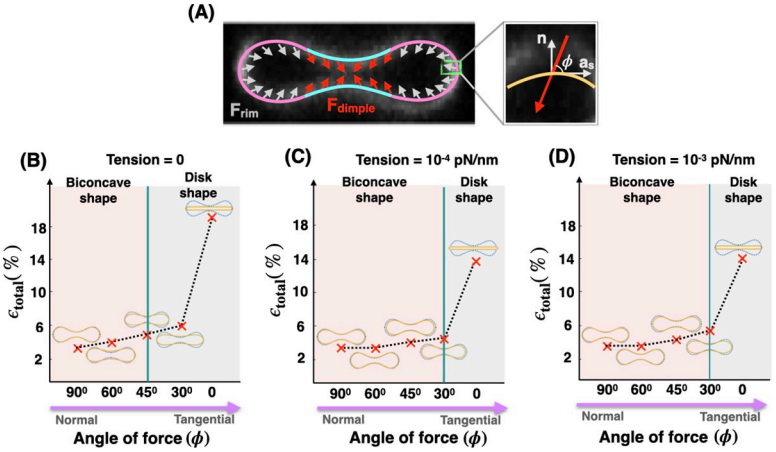

Fig 8. The role of tension and angle of applied forces. Effective membrane tension and the angle of applied forces in the RBC dimple and rim regions work together to maintain the biconcave shape of an RBC. (A) Schematic of a biconcave RBC with a non-uniform distribution of force density across the dimple and rim regions. In both regions, the forces per unit area are applied with angle ϕ with respect to the tangent vector ($\mathbf{a_s}$). (B-D) The shape error and the RBC shapes obtained from simulation for different angles of the applied forces (ϕ) for (B) tensionless membrane, (C) low tension (tension = 10^{-4} pN/nm), and (D) intermediate tension (tension = 10^{-3} pN/nm). For all values of the membrane tension, as the angle of forces deviates from normal ($\phi = 90^0$) to tangential orientation ($\phi = 0$), the simulated shapes flatten and the shape error increases.

https://doi.org/10.1371/journal.pcbi.1007890.g008

membrane tension (Fig 8C and 8D). Finally, in the case of high membrane tension, as expected from Fig 7C, independent of the angle of force ϕ, the simulated shapes have a pancake-shaped morphology with very large shape errors (see S9 Fig). Thus our model predicts that membrane tension and the orientation of the applied forces can be collectively tuned to actively maintain the biconcave morphology of an RBC.

Discussion

The biconcave disk shape of mammalian RBCs provides a maximum surface-area-to-volume ratio, which enables efficient gas and ion exchange and increases RBC deformability and resiliency [99]. This shape has been studied extensively from a mechanical standpoint to identify stress-strain relationships in cell membranes. Most studies modeling RBC shapes have been based on the work of Canham and Helfrich [59,65] and have reinforced the idea that mechanical force balance on the membrane by itself can provide insights into the unique shape of the RBC. The studies by Canham and Helfrich and other researchers suggested that the minimization of the membrane bending energy and the asymmetry between the inner and outer membrane leaflets generate the RBC biconcavity [30,31]. For example, Markin showed how the induced nano-scale curvature field due to the lateral distribution of membrane components can prescribe the biconcave shape of RBCs [36]. Here, we focused on micron-scale differences in lateral distribution of myosin-mediated forces as another degree of freedom and demonstrated how they are important for maintaining the RBC biconcave shape.

In RBCs, the skeleton underneath the plasma membrane is an elastic network of spectrin linked to short actin filament nodes that are attached to the membrane by anchoring proteins [26,27]. Studies of human and mouse congenital hemolytic anemias have also established a role for the RBC membrane skeleton in maintaining RBC biconcave shape in circulation [23,24,26]. Many different studies have demonstrated the importance of membrane/skeleton interactions in the formation of unusual RBC shapes as well as RBC deformability in the shear flow [49,100–102]. In these studies, the RBC lipid bilayer and the membrane skeleton were mainly modeled as two distinct elastic components connected to each other via bond proteins [45–47]. However, no theoretical models for RBC biconcave shape have considered an active role for mechanochemical forces due to myosin motor proteins interacting with membrane skeleton F-actin in regulating RBC morphologies [45,103].

A recent study by Smith et al. [53] highlighted a critical role for NMIIA interactions with F-actin in the membrane skeleton in controlling RBC membrane tension and curvature. This discovery of a new experimental phenomenon calls for explanation and new/modified models that explicitly incorporate the effects of the molecular motors into the models based on pure membrane mechanics. Ultimately, RBCs can be used as a simple model system to explore the general role of NMII-generated forces in regulating plasma membrane curvature since RBC are the only cell type where F-actin is exclusively in the membrane skeleton [26]. The ubiquity of the membrane skeleton at the plasma membranes of all metazoan cells, where F-actin is also present in a transcellular cytoskeleton, further emphasizes the utility of the RBC paradigm.

In this study, we revisited the classical Helfrich-Canham energy model for the RBC membrane to include non-uniform forces along the membrane due to NMIIA-actin interactions. Undoubtedly, adding an additional degree of freedom to the energy allows us to attain a better match between the simulated and the experimentally observed RBC shapes compared to previous studies. Further, based on our results, we predicted two conditions that need to be satisfied to produce the best fit with the experimental shapes of RBCs. First, the density of the NMIIA-generated force must be non-uniform along the RBC membrane to produce the best fit with the shapes measured experimentally. By conducting a parameter sweep of the force density

configurations, we found that the non-uniform force distribution must be such that F_{dimple} is larger than F_{rim} (Figs 4 and 5). Experimental measurements of NMIIA density in the dimple and rim regions of RBCs using immunofluorescence showed that indeed NMIIA density is higher in the dimple than in the rim (Fig 6) by about 25%. Our combined computational and experimental results highlight that a micron-scale, non-uniform force distribution of NMIIA plays a fundamental role in maintaining the biconcave shape of RBCs. We emphasize that this non-uniform density of forces is at the length scale of microns rather than at the length scale of fluctuations of the RBC membrane [104].

Second, we predicted that the effective membrane tension and the orientation of the applied forces are important physical parameters in modulating the RBC morphology and the required NMIIA-mediated force density ratio in the RBC dimple versus the rim region (F_{ratio}) (Figs 7 and 8). As compared to tensionless or low-tension membranes, the intermediate tension values F_{ratio} for minimum shape error (~1.27) are a better match with the experimentally reported NMIIA density ratio at the dimple versus the rim. Furthermore, we found that the deviation of the applied forces from normal to tangential orientations results in pancake-shaped morphologies with very large shape errors compared to the actual biconcave shape of RBCs (Fig 8). Additionally, we calculated the reduced volume (υ); the volume of the simulated RBC with respect to the volume of the sphere with no force (Eq. S14). Based on our calculation, the reduced volume of biconcave RBC varies in a wide range between ~0.62 and 0.83. A recent study by Mesarec et al. has also shown that in stable discocyte RBS shapes, the reduced volume varies in a wide range (between 0.58 and 0.8) if the membrane's in-plane ordering is taken into account [105]

Therefore, we predict that in mature, healthy biconcave RBCs, NMIIA motor domains exert force on the membrane with angle $\phi > 30^0$ under intermediate membrane tension ($\sim 10^{-2}$ pN/nm) and the reduced volume can vary in a broad range. Currently, the exact value of membrane tension and the angle of forces in an intact RBC are hard to measure because of the contributions from both the membrane and the underlying skeleton [106,107]. In the literature, a wide range of values are reported for the membrane tension from 10^{-1} pN/nm to 10^{-4} pN/nm [70,93,96]. This range can be attributed to dynamic lipid rearrangements [108], membrane-skeleton interactions [109], and based on our work here, rearrangement of force-generating NMIIA molecules [53]. The angle of applied forces by NMIIA at the RBC membrane is still a matter of debate because nanoscale 3D images of F-actin and NMIIA motors using cryoelectron tomograms would be required to explore the relative configurations of myosin motors, F-actin and the RBC membrane surface [107]. This will require the development of novel sample preparation approaches for RBCs and is a subject for future study. Our theoretical analyses, supported by experimental measurements, implicitly suggest that for a biconcave RBC, the effective membrane tension should be on the order of 10^{-2} pN/nm and the NMIIA motors should apply forces with angles $\phi > 30^0$ with respect to the membrane surface.

Our conclusions of non-uniform force density and tension regulation can be used to obtain insight into the effective activity of NMIIA motor domains at any given time. Assuming that a single NMIIA motor domain produces an average force of ~ 2 pN [110,111], the calculated force densities (calculated using force per unit volume) in Fig 7B corresponds to 90 and 815 myosin motor domains in the dimple and rim regions, respectively. This means that the force generated by a total of ~850 active NMIIA motor domains, distributed between the dimple and the rim as we predicted, is sufficient to sustain the biconcave disk shape of an RBC. Previous studies estimated that each mature human RBC contains ~ 6,000 NMIIA molecules, ~12,000 motor domains [50,51] and at any given time, roughly 40–50% of these molecules are bound to the membrane skeleton [53]. Our calculations suggest that approximately 15% of these bound NMIIA molecules are active and exerting forces distributed unevenly along the

membrane. It is also possible that the amount of force generated by a single NMIIA motor domain varies due to the stiffness of the membrane skeleton network, the processivity (the duration over which the motor stays attached to actin), and the cross-linking activity of NMIIA myosin filaments [110,111]. Therefore, further research will be required to determine the quantitative relationship between the copy number of NMIIA molecules and their activity, that together determine the overall magnitude of the force exerted on the RBC membrane.

The idea of the asymmetrical distribution of the membrane skeleton and its components in the dimple and rim areas of RBCs was initially introduced by Hoffman, although no direct evidence for this was obtained [112,113]. Recently, Svetina et al. modeled RBC volume regulation according to the permeability of the Piezo1 channel. Based on their simulation results, they found that Piezo1 channels are expected to be distributed non-uniformly in a biconcave RBC, tending to localize in the dimple region [114]. They speculated that the simulated localization of Piezo1 channels in the dimple region is controlled by the membrane curvature and induced surface tractions [115]. The RBC membrane curvature may also influence the localization of NMIIA motor proteins, as has been observed in other cell types [15]. Alternatively, a shear-induced Ca^{2+} influx through localized Piezo1 channels could locally activate NMIIA through activation of myosin light chain kinase and phosphorylation of the regulatory light chain [50–52], leading to enhanced NMIIA binding to F-actin and enhanced local contractility at the dimple, activating Piezo1 and Ca^{2+} influx in a feed-forward loop. We believe our findings here are a motivation for future studies to develop quantitative relationships between the myosin-mediated forces, Ca^{2+} influxes, and the membrane curvature of the cell surface.

We acknowledge that despite the conclusions from our studies, there are some limitations and simplifying assumptions that will need to be revisited for future studies. First, we limited our model to axisymmetric shapes, while RBCs often adopt non-axisymmetric shapes [116]. Future studies will involve simulations without any assumptions of symmetry [117]. Experimental tests probing whether NMIIA activity is non-uniform along the RBC membrane will also give insight into NMIIA density distribution versus activity distribution along the membrane. Second, we assumed that the contributions from thermal fluctuations and the deformation of the membrane skeleton are negligible compared to the bending energy [61,118]. However, for a more general quantitative model, these effects should be considered [104]. Particularly, in the case of discocyte-echinocyte RBC shape transformation and in RBC membrane vesiculation, previous studies have shown the important role of membrane skeleton in driving these shape transformations [48,49,119–122]. Future efforts focusing on the shape transformations of RBCs from discocytes to echinocytes or stomatocytes will be important to connect RBC morphology to physiological function and molecular mechanisms. There is also an opportunity to extend the current models for non biconcave RBCs shape including experimental manipulation of the membrane tension or inhibition of the myosin activity in RBCs [106,123,124]. These require the adaptation of newly emerging technologies for RBC biology and will provide new insight into the molecular mechanisms of RBC shape generation and maintenance.

Materials and methods

a. **Immunofluorescence staining of RBCs.** Human peripheral whole blood was collected from healthy human donors into EDTA tubes (BD Diagnostics). 20μl of whole blood was added to 1 ml of 4% paraformaldehyde (PFA, Electron Microscopy Sciences) in Dulbecco's PBS (DPBS–Gibco), mixed, and incubated at room temperature overnight.

   i. **NMIIA immunostaining and rhodamine phalloidin staining.** Fixed RBCs were washed three times in DPBS by centrifuging for 5 minutes at 1000 x *g*, permeabilized in

DPBS + 0.3% TX-100 for 10 minutes, and then blocked in 4% BSA, 1% normal goat serum in DPBS (Blocking Buffer, BB) at 4˚C for at least 4 days or up to 1 week before immunostaining. Permeabilized and blocked RBCs were then incubated with rabbit anti-NMIIA motor domain antibody (Abcam ab75590) diluted in BB (1:1000) for 2–3 hours at room temperature, washed two times in BB as above, and then incubated in Alexa-488-conjugated goat anti-rabbit secondary antibody (Life Technologies A11008, diluted 1:1000) mixed with rhodamine-phalloidin (Life Technologies R415, at a final concentration of 130nM) in BB for 1–2 hr at room temperature, followed by washing three times in BB as above. Stained cells were cytospun onto slides and mounted with ProLong™ Gold mounting medium (Invitrogen) and coverslipped prior to imaging.

ii. **Glycophorin A (GPA) immunostaining.** Fixed RBCs were washed three times in DPBS by centrifuging for 5 minutes at 1000 x *g*, blocked for 1 hour in BB, and stained with FITC-conjugated mouse anti-GPA antibody (BD Pharmingen 559943) for 1 hour at room temperature. GPA-stained RBCs were washed twice in DPBS by centrifugation as above, then cytospun onto glass slides and mounted with Prolong™ Gold and coverslipped prior to imaging.

b. **Fluorescence microscopy.**

i. **RBCs immunostained for NMIIA and rhodamine phalloidin for F-actin.** RBCs were imaged using a Zeiss LSM 880 Airyscan laser scanning confocal microscope with a 63× 1.46 NA oil Plan Apo objective. Z-stacks were acquired at a digital zoom of 1.8 and a Z-step size of 0.168 μm. The distance between Z-steps was set to 0.10 μm in images used for NMIIA puncta analysis in Volocity (Quorum Technologies).

ii. **RBCs immunostained for NMIIA and rhodamine phalloidin for F-actin.** RBCs were imaged using a Zeiss LSM 880 Airyscan laser scanning confocal microscope with a 63× 1.46 NA oil Plan Apo objective. Z-stacks were acquired at a digital zoom of 1.8 and a Z-step size of 0.168 μm.

iii. **RBCs immunostained for GPA.** RBCs were imaged using a Zeiss LSM 780 laser scanning confocal microscope with a 100× 1.4 NA oil Plan Apo objective. Z-stacks were acquired at a digital zoom of 1.0 and a Z-step size of 0.25 μm. The distance between Z-steps was set to 0.18 μm in images used for presentation.

c. **Image analysis.** Numbers of NMIIA puncta in whole RBCs, in the dimples, and in the rims were counted automatically from Airyscan confocal stacks in Volocity (Quorum Technologies) using the "Find Spots" function in the "Measurements" module. The volumes of whole RBCs, the dimples, and the rims were measured from the rhodamine phalloidin (F-actin) fluorescence in Volocity using the "Find Objects" function, with gaps in staining filled using the "Close" function. RBC height measurements were acquired manually from XZ views of the center of each RBC in Volocity using the line function to measure the distance between the edges of fluorescent F-actin staining signal at the widest and narrowest regions of each RBC.

d. **Statistical analysis.** Data are presented in dot plots as mean ± standard deviation (SD), or in scatter plots showing the best-fit line from the linear regression. Differences between the variances of the two samples were detected using F-tests. Differences between means were detected using unpaired t-tests with Welch's correction. When more than one comparison was made, differences between means were detected using one-way ANOVA followed by Tukey's multiple comparisons test. Statistical significance was defined as $p < 0.05$. Statistical analysis was performed using GraphPad Prism 7.03 software.

Supporting information

S1 Fig. The shape error in the characteristic length scales of RBC is a nonlinear function of dimple force density.
(PDF)

S2 Fig. Applying a large pulling force at the RBC rim region causes a very large shape error.
(PDF)

S3 Fig. Applying a large pushing force at the RBC rim region increases the total shape error.
(PDF)

S4 Fig. The number of NMIIA puncta increases with region volume.
(PDF)

S5 Fig. RBCs with higher biconcavity have higher NMIIA density in the whole RBC and in the dimple region.
(PDF)

S6 Fig. For tensionless membrane, deviation of the applied forces from normal to the tangential orientation results in the formation of pancake-shaped geometries with large shape error.
(PDF)

S7 Fig. For low membrane tension, deviation of the applied forces from normal to the tangential orientation results in the formation of pancake-shaped geometries with large shape error.
(PDF)

S8 Fig. For intermediate membrane tension, deviation of the applied forces from normal to the tangential orientation results in the formation of pancake-shaped geometries with large shape error.
(PDF)

S9 Fig. For high membrane tension, independent of the orientation of the force, the simulated shapes have pancake morphologies and the shape error is large.
(PDF)

S1 Table. Table of notations used in the model.
(PDF)

S2 Table. Table of notations used in the model.
(PDF)

S1 Text. Details of the mathematical model.
(PDF)

Acknowledgments

We would like to thank Ms. Miriam Bell, Ms. Jennifer Fromm, and Dr. Christopher Lee for insightful comments and suggestions for improving this manuscript.

Author Contributions

Conceptualization: Haleh Alimohamadi, Alyson S. Smith, Roberta B. Nowak, Velia M. Fowler, Padmini Rangamani.

Data curation: Haleh Alimohamadi, Alyson S. Smith, Roberta B. Nowak.

Formal analysis: Haleh Alimohamadi, Alyson S. Smith, Roberta B. Nowak, Velia M. Fowler, Padmini Rangamani.

Funding acquisition: Velia M. Fowler, Padmini Rangamani.

Investigation: Haleh Alimohamadi, Alyson S. Smith.

Methodology: Haleh Alimohamadi, Alyson S. Smith.

Software: Haleh Alimohamadi, Alyson S. Smith.

Supervision: Velia M. Fowler, Padmini Rangamani.

Validation: Haleh Alimohamadi, Alyson S. Smith, Roberta B. Nowak.

Writing – original draft: Haleh Alimohamadi, Alyson S. Smith, Padmini Rangamani.

Writing – review & editing: Haleh Alimohamadi, Alyson S. Smith, Roberta B. Nowak, Velia M. Fowler, Padmini Rangamani.

References

1. Singhvi R, Kumar A, Lopez GP, Stephanopoulos GN, Wang DI, Whitesides GM, et al. Engineering cell shape and function. Science. 1994; 264: 696–698.
2. Rangamani P, Lipshtat A, Azeloglu EU, Calizo RC, Hu M, Ghassemi S, et al. Decoding information in cell shape. Cell. 2013; 154: 1356–1369.
3. Murrell M, Oakes PW, Lenz M, Gardel ML. Forcing cells into shape: the mechanics of actomyosin contractility. Nat Rev Mol Cell Biol. 2015; 16: 486–498.
4. Paluch E, Sykes C, Prost J, Bornens M. Dynamic modes of the cortical actomyosin gel during cell locomotion and division. Trends Cell Biol. 2006; 16: 5–10.
5. Salbreux G, Charras G, Paluch E. Actin cortex mechanics and cellular morphogenesis. Trends Cell Biol. 2012; 22: 536–545.
6. Vicente-Manzanares M, Ma X, Adelstein RS, Horwitz AR. Non-muscle myosin II takes centre stage in cell adhesion and migration. Nat Rev Mol Cell Biol. 2009; 10: 778–790.
7. Heissler SM, Manstein DJ. Nonmuscle myosin-2: mix and match. Cell Mol Life Sci. 2013; 70: 1–21.
8. Conti MA, Adelstein RS. Nonmuscle myosin II moves in new directions. J Cell Sci. 2008; 121: 11–18.
9. Agarwal P, Zaidel-Bar R. Principles of Actomyosin Regulation In Vivo. Trends Cell Biol. 2019; 29: 150–163.
10. Gorfinkiel N, Blanchard GB. Dynamics of actomyosin contractile activity during epithelial morphogenesis. Curr Opin Cell Biol. 2011; 23: 531–539.
11. Kasza KE, Zallen JA. Dynamics and regulation of contractile actin-myosin networks in morphogenesis. Curr Opin Cell Biol. 2011; 23: 30–38.
12. Lecuit T, Lenne P-F, Munro E. Force generation, transmission, and integration during cell and tissue morphogenesis. Annu Rev Cell Dev Biol. 2011; 27: 157–184.
13. Yamada KM, Sixt M. Mechanisms of 3D cell migration. Nat Rev Mol Cell Biol. 2019. https://doi.org/10.1038/s41580-019-0172-9 PMID: 31582855
14. Kalluri R, Weinberg RA. The basics of epithelial-mesenchymal transition. J Clin Invest. 2009; 119: 1420–1428.
15. Lyons SM, Alizadeh E, Mannheimer J, Schuamberg K, Castle J, Schroder B, et al. Changes in cell shape are correlated with metastatic potential in murine and human osteosarcomas. Biol Open. 2016; 5: 289–299.
16. Suresh S, Spatz J, Mills JP, Micoulet A, Dao M, Lim CT, et al. Connections between single-cell biomechanics and human disease states: gastrointestinal cancer and malaria. Acta Biomater. 2005; 1: 15–30.
17. Pecci A, Ma X, Savoia A, Adelstein RS. MYH9: Structure, functions and role of non-muscle myosin IIA in human disease. Gene. 2018; 664: 152–167.

18. Schell C, Sabass B, Helmstaedter M, Geist F, Abed A, Yasuda-Yamahara M, et al. ARP3 Controls the Podocyte Architecture at the Kidney Filtration Barrier. Dev Cell. 2018; 47: 741–757.e8.
19. Tousley A, Iuliano M, Weisman E, Sapp E, Zhang N, Vodicka P, et al. Rac1 Activity Is Modulated by Huntingtin and Dysregulated in Models of Huntington's Disease. J Huntingtons Dis. 2019; 8: 53–69.
20. Elliott H, Fischer RS, Myers KA, Desai RA, Gao L, Chen CS, et al. Myosin II controls cellular branching morphogenesis and migration in three dimensions by minimizing cell-surface curvature. Nat Cell Biol. 2015; 17: 137–147.
21. Diez-Silva M, Dao M, Han J, Lim C-T, Suresh S. Shape and Biomechanical Characteristics of Human Red Blood Cells in Health and Disease. MRS Bull. 2010; 35: 382–388.
22. Bronner F. Cell Shape: Determinants, Regulation, And Regulatory Role. Elsevier; 2012.
23. Mohandas N, Evans E. Mechanical properties of the red cell membrane in relation to molecular structure and genetic defects. Annu Rev Biophys Biomol Struct. 1994; 23: 787–818.
24. Mohandas N, Gallagher PG. Red cell membrane: past, present, and future. Blood. 2008; 112: 3939–3948.
25. Chien S. Red cell deformability and its relevance to blood flow. Annu Rev Physiol. 1987; 49: 177–192.
26. Fowler VM. Chapter Two—The Human Erythrocyte Plasma Membrane: A Rosetta Stone for Decoding Membrane–Cytoskeleton Structure. In: Bennett V, editor. Current Topics in Membranes. Academic Press; 2013. pp. 39–88.
27. Gratzer WB. The red cell membrane and its cytoskeleton. Biochem J. 1981; 198: 1–8.
28. Gokhin DS, Fowler VM. Feisty filaments: actin dynamics in the red blood cell membrane skeleton. Curr Opin Hematol. 2016; 23: 206–214.
29. Discher DE. New insights into erythrocyte membrane organization and microelasticity. Curr Opin Hematol. 2000; 7: 117–122.
30. Canham PB. The minimum energy of bending as a possible explanation of the biconcave shape of the human red blood cell. J Theor Biol. 1970; 26: 61–81.
31. Helfrich W. Elastic properties of lipid bilayers: theory and possible experiments. Z Naturforsch C. 1973; 28: 693–703.
32. Deuling HJ, Helfrich W. The curvature elasticity of fluid membranes: A catalogue of vesicle shapes. Journal de Physique. 1976; 37: 1335–1345.
33. Deuling HJ, Helfrich W. Red blood cell shapes as explained on the basis of curvature elasticity. Biophys J. 1976; 16: 861–868.
34. Sheetz MP, Singer SJ. Biological membranes as bilayer couples. A molecular mechanism of drug-erythrocyte interactions. Proc Natl Acad Sci U S A. 1974; 71: 4457–4461.
35. Iglič A, Kralj-Iglič V, Hägerstrand H. Amphiphile induced echinocyte-spheroechinocyte transformation of red blood cell shape. Eur Biophys J. 1998; 27: 335–339.
36. Markin VS. Lateral organization of membranes and cell shapes. Biophys J. 1981; 36: 1–19.
37. Leibler S. Curvature instability in membranes. Journal de Physique. 1986; 47: 507–516.
38. Andelman D, Kawakatsu T, Kawasaki K. Equilibrium shape of two-component unilamellar membranes and vesicles. EPL. 1992; 19: 57.
39. Kralj-Iglič V, Svetina S, Žekž B. Shapes of bilayer vesicles with membrane embedded molecules. Eur Biophys J. 1996; 24: 311–321.
40. Iglič A, Fošnarič M, Hägerstrand H, Kralj-Iglič V. Coupling between vesicle shape and the non-homogeneous lateral distribution of membrane constituents in Golgi bodies. FEBS Lett. 2004; 574: 9–12.
41. Tachikawa M, Mochizuki A. Golgi apparatus self-organizes into the characteristic shape via postmitotic reassembly dynamics. Proc Natl Acad Sci U S A. 2017; 114: 5177–5182.
42. Walani N, Torres J, Agrawal A. Anisotropic spontaneous curvatures in lipid membranes. Phys Rev E Stat Nonlin Soft Matter Phys. 2014; 89: 062715.
43. Fošnarič M, Penič S, Iglič A, Kralj-Iglič V, Drab M, Gov NS. Theoretical study of vesicle shapes driven by coupling curved proteins and active cytoskeletal forces. Soft Matter. 2019; 15: 5319–5330.
44. Gov NS. Guided by curvature: shaping cells by coupling curved membrane proteins and cytoskeletal forces. Philos Trans R Soc Lond B Biol Sci. 2018; 373. https://doi.org/10.1098/rstb.2017.0115 PMID: 29632267
45. Peng Z, Li X, Pivkin IV, Dao M, Karniadakis GE, Suresh S. Lipid bilayer and cytoskeletal interactions in a red blood cell. Proc Natl Acad Sci U S A. 2013; 110: 13356–13361.
46. Park Y, Best CA, Auth T, Gov NS, Safran SA, Popescu G, et al. Metabolic remodeling of the human red blood cell membrane. Proc Natl Acad Sci U S A. 2010; 107: 1289–1294.

47. Li J, Lykotrafitis G, Dao M, Suresh S. Cytoskeletal dynamics of human erythrocyte. Proc Natl Acad Sci U S A. 2007; 104: 4937–4942.
48. Iglic A. A possible mechanism determining the stability of spiculated red blood cells. J Biomech. 1997; 30: 35–40.
49. Mukhopadhyay R, Lim H W G, Wortis M. Echinocyte shapes: bending, stretching, and shear determine spicule shape and spacing. Biophys J. 2002; 82: 1756–1772.
50. Fowler VM, Davis JQ, Bennett V. Human erythrocyte myosin: identification and purification. J Cell Biol. 1985; 100: 47–55.
51. Wong AJ, Kiehart DP, Pollard TD. Myosin from human erythrocytes. J Biol Chem. 1985; 260: 46–49.
52. Higashihara M, Hartshorne DJ, Craig R, Ikebe M. Correlation of enzymatic properties and conformation of bovine erythrocyte myosin. Biochemistry. 1989; 28: 1642–1649.
53. Smith AS, Nowak RB, Zhou S, Giannetto M, Gokhin DS, Papoin J, et al. Myosin IIA interacts with the spectrin-actin membrane skeleton to control red blood cell membrane curvature and deformability. Proc Natl Acad Sci U S A. 2018; 115: E4377–E4385.
54. Rawicz W, Olbrich KC, McIntosh T, Needham D, Evans E. Effect of chain length and unsaturation on elasticity of lipid bilayers. Biophys J. 2000; 79: 328–339.
55. Steigmann DJ. Fluid Films with Curvature Elasticity. Arch Ration Mech Anal. 1999; 150: 127–152.
56. Rangamani P, Agrawal A, Mandadapu KK, Oster G, Steigmann DJ. Interaction between surface shape and intra-surface viscous flow on lipid membranes. Biomech Model Mechanobiol. 2013; 12: 833–845.
57. Rangamani P, Mandadap KK, Oster G. Protein-induced membrane curvature alters local membrane tension. Biophys J. 2014; 107: 751–762.
58. Jenkins J. The Equations of Mechanical Equilibrium of a Model Membrane. SIAM J Appl Math. 1977; 32: 755–764.
59. Jenkins JT. Static equilibrium configurations of a model red blood cell. J Math Biol. 1977; 4: 149–169.
60. Pai BK, Weymann HD. Equilibrium shapes of red blood cells in osmotic swelling. J Biomech. 1980; 13: 105–112.
61. Lim H. W. G, Wortis M, Mukhopadhyay R. Red Blood Cell Shapes and Shape Transformations: Newtonian Mechanics of a Composite Membrane: Sections 2.1–2.4. In: Gompper G, Schick M, editors. Soft Matter. Weinheim, Germany: Wiley-VCH Verlag GmbH & Co. KGaA; 2008. pp. 83–139.
62. Mohandas N, Chasis JA. Red blood cell deformability, membrane material properties and shape: regulation by transmembrane, skeletal and cytosolic proteins and lipids. Semin Hematol. 1993; 30: 171–192.
63. Fung YC, Tong P. Theory of the sphering of red blood cells. Biophys J. 1968; 8: 175–198.
64. Park H, Lee S, Ji M, Kim K, Son Y, Jang S, et al. Measuring cell surface area and deformability of individual human red blood cells over blood storage using quantitative phase imaging. Sci Rep. 2016; 6: 34257.
65. Luke J. A Method for the Calculation of Vesicle Shapes. SIAM J Appl Math. 1982; 42: 333–345.
66. Svetina S, Zeks B. Membrane bending energy and shape determination of phospholipid vesicles and red blood cells. Eur Biophys J. 1989; 17: 101–111.
67. Walani N, Torres J, Agrawal A. Endocytic proteins drive vesicle growth via instability in high membrane tension environment. Proc Natl Acad Sci U S A. 2015; 112: E1423–32.
68. Derényi I, Jülicher F, Prost J. Formation and interaction of membrane tubes. Phys Rev Lett. 2002; 88: 238101.
69. Alimohamadi H, Rangamani P. Modeling Membrane Curvature Generation due to Membrane–Protein Interactions. Biomolecules. 2018; 8: 120.
70. Rand RP, Burton AC. MECHANICAL PROPERTIES OF THE RED CELL MEMBRANE. I. MEMBRANE STIFFNESS AND INTRACELLULAR PRESSURE. Biophys J. 1964; 4: 115–135.
71. Agrawal A, Steigmann DJ. Modeling protein-mediated morphology in biomembranes. Biomech Model Mechanobiol. 2009; 8: 371–379.
72. Alimohamadi H, Ovryn B, Rangamani P. Modeling membrane nanotube morphology: the role of heterogeneity in composition and material properties. https://doi.org/10.1101/373811
73. Canham PB, Burton AC. Distribution of size and shape in populations of normal human red cells. Circ Res. 1968; 22: 405–422.
74. Chien S, Usami S, Dellenback RJ, Bryant CA. Comparative hemorheology—hematological implications of species differences in blood viscosity. Biorheology. 1971; 8: 35–57.

75. Evans E, Fung YC. Improved measurements of the erythrocyte geometry. Microvasc Res. 1972; 4: 335–347.

76. Fung YC, Tsang WC, Patitucci P. High-resolution data on the geometry of red blood cells. Biorheology. 1981; 18: 369–385.

77. Richieri GV, Akeson SP, Mel HC. Measurement of biophysical properties of red blood cells by resistance pulse spectroscopy: volume, shape, surface area, and deformability. J Biochem Biophys Methods. 1985; 11: 117–131.

78. Linderkamp O, Friederichs E, Meiselman HJ. Mechanical and geometrical properties of density-separated neonatal and adult erythrocytes. Pediatr Res. 1993; 34: 688–693.

79. Engström KG, Meiselman HJ. Optical and mathematical corrections of micropipette measurements of red blood cell geometry during anisotonic perifusion. Cytometry. 1994; 17: 279–286.

80. Tycko DH, Metz MH, Epstein EA, Grinbaum A. Flow-cytometric light scattering measurement of red blood cell volume and hemoglobin concentration. Appl Opt. 1985; 24: 1355.

81. Tarasov P, Yurkin M, Avrorov P, Semyanov K, Hoekstra A, Maltsev V. OPTICS OF ERYTHROCYTES. Optics of Biological Particles. Springer Netherlands; 2007. pp. 243–259.

82. Ergül Ö, Arslan-Ergül A, Gürel L. Computational study of scattering from healthy and diseased red blood cells. J Biomed Opt. 2010. Available: https://www.spiedigitallibrary.org/journals/Journal-of-Biomedical-Optics/volume-15/issue-4/045004/Computational-study-of-scattering-from-healthy-and-diseased-red-blood/10.1117/1.3467493.short

83. Das M, Das B, Das A, Chatterjee I, Majumder D. Computational analysis of ultrastructural images of red blood cells. Journal of Oncology Translational Research. 2015; 1: 103.

84. Funaki H. Contributions on the shapes of red blood corpuscles. Jpn J Physiol. 1955; 5: 81–92.

85. Kuchel PW, Fackerell ED. Parametric-equation representation of biconcave erythrocytes. Bull Math Biol. 1999; 61: 209–220.

86. Yurkin MA. Discrete dipole simulations of light scattering by blood cells. Universiteit van Amsterdam. 2007. Available: https://dare.uva.nl/search?identifier=2df63a32-fc98-479c-8bfc-0cb95163574b

87. Borovoi AG, Naats EI, Oppel UG. Scattering of light by a red blood cell. J Biomed Opt. 1998; 3: 364–372.

88. Bi L, Yang P. Modeling of light scattering by biconcave and deformed red blood cells with the invariant imbedding T-matrix method. J Biomed Opt. 2013; 18: 55001.

89. Yurkin MA, Semyanov KA, Tarasov PA, Chernyshev AV, Hoekstra AG, Maltsev VP. Experimental and theoretical study of light scattering by individual mature red blood cells by use of scanning flow cytometry and a discrete dipole approximation. Appl Opt. 2005; 44: 5249–5256.

90. Lyu J, Chen PG, Boedec G, Leonetti M, Jaeger M. Hybrid continuum–coarse-grained modeling of erythrocytes. Comptes Rendus Mécanique. 2018; 346: 439–448.

91. Evans EA. Mechanics and Thermodynamics of Biomembranes: 0. 2018. Available: https://content.taylorfrancis.com/books/download?dac=C2017-0-66844-1&isbn=9781351082785&format=googlePreviewPdf

92. Lewis AH, Grandl J. Mechanical sensitivity of Piezo1 ion channels can be tuned by cellular membrane tension. Elife. 2015; 4. https://doi.org/10.7554/eLife.12088 PMID: 26646186

93. Evans J, Gratzer W, Mohandas N, Parker K, Sleep J. Fluctuations of the red blood cell membrane: relation to mechanical properties and lack of ATP dependence. Biophys J. 2008; 94: 4134–4144.

94. Shi Z, Graber ZT, Baumgart T, Stone HA, Cohen AE. Cell Membranes Resist Flow. Cell. 2018; 175: 1769–1779.e13.

95. Huff J. The Airyscan detector from ZEISS: confocal imaging with improved signal-to-noise ratio and super-resolution. Nat Methods. 2015; 12. Available: https://www.nature.com/articles/nmeth.f.388.pdf?origin=ppub

96. Popescu G, Ikeda T, Goda K, Best-Popescu CA, Laposata M, Manley S, et al. Optical measurement of cell membrane tension. Phys Rev Lett. 2006; 97: 218101.

97. Diz-Muñoz A, Fletcher DA, Weiner OD. Use the force: membrane tension as an organizer of cell shape and motility. Trends Cell Biol. 2013; 23: 47–53.

98. Molloy JE, Burns JE, Kendrick-Jones J, Tregear RT, White DC. Movement and force produced by a single myosin head. Nature. 1995; 378: 209–212.

99. Hodgkin Lister JJ. XXVI. Notice of some miscroscopic observations of the blood and animal tissues. Philos Mag. 1827; 2: 130–138.

100. Kuzman D, Svetina S, Waugh RE, Zeks B. Elastic properties of the red blood cell membrane that determine echinocyte deformability. Eur Biophys J. 2004; 33: 1–15.

101. Peng Z, Asaro RJ, Zhu Q. Multiscale simulation of erythrocyte membranes. Phys Rev E Stat Nonlin Soft Matter Phys. 2010; 81: 031904.

102. Pivkin IV, Peng Z, Karniadakis GE, Buffet PA, Dao M, Suresh S. Biomechanics of red blood cells in human spleen and consequences for physiology and disease. Proc Natl Acad Sci U S A. 2016; 113: 7804–7809.

103. Peng Z, Mashayekh A, Zhu Q. Erythrocyte responses in low-shear-rate flows: effects of non-biconcave stress-free state in the cytoskeleton. J Fluid Mech. 2014; 742: 96–118.

104. Gov NS, Safran SA. Red blood cell membrane fluctuations and shape controlled by ATP-induced cytoskeletal defects. Biophys J. 2005; 88: 1859–1874.

105. Mesarec L, Góźdź W, Iglič A, Kralj-Iglič V, Virga EG, Kralj S. Normal red blood cells' shape stabilized by membrane's in-plane ordering. Sci Rep. 2019; 9: 19742.

106. Colom A, Derivery E, Soleimanpour S, Tomba C, Molin MD, Sakai N, et al. A fluorescent membrane tension probe. Nat Chem. 2018; 10: 1118–1125.

107. Lan G, Sun SX. Dynamics of myosin-driven skeletal muscle contraction: I. Steady-state force generation. Biophys J. 2005; 88: 4107–4117.

108. Jähnig F. What is the surface tension of a lipid bilayer membrane? Biophys J. 1996; 71: 1348–1349.

109. Sheetz MP. Membrane skeletal dynamics: role in modulation of red cell deformability, mobility of transmembrane proteins, and shape. Semin Hematol. 1983; 20: 175–188.

110. Norstrom MF, Smithback PA, Rock RS. Unconventional processive mechanics of non-muscle myosin IIB. J Biol Chem. 2010; 285: 26326–26334.

111. Hundt N, Steffen W, Pathan-Chhatbar S, Taft MH, Manstein DJ. Load-dependent modulation of non-muscle myosin-2A function by tropomyosin 4.2. Sci Rep. 2016; 6: 20554.

112. Hoffman JF. Biconcave shape of human red-blood-cell ghosts relies on density differences between the rim and dimple of the ghost's plasma membrane. Proc Natl Acad Sci U S A. 2016; 113: 14847–14851.

113. Hoffman JF. Evidence that asymmetry of the membrane/cytoskeletal complex in human red blood cell ghosts is responsible for their biconcave shape. Proc Natl Acad Sci U S A. 2018; 115: 1641–1645.

114. Svetina S, Švelc Kebe T, Božič B. A Model of Piezo1-Based Regulation of Red Blood Cell Volume. Biophys J. 2019; 116: 151–164.

115. Alimohamadi H, Vasan R, Hassinger JE, Stachowiak JC, Rangamani P. The role of traction in membrane curvature generation. Mol Biol Cell. 2018; 29: 2024–2035.

116. Kaoui B, Biros G, Misbah C. Why do red blood cells have asymmetric shapes even in a symmetric flow? Phys Rev Lett. 2009; 103: 188101.

117. Vasan R, Rudraraju S, Akamatsu M, Garikipati K, Rangamani P. A mechanical model reveals that non-axisymmetric buckling lowers the energy barrier associated with membrane neck constriction. Soft Matter. 2020; 16: 784–797.

118. Svetina S, Kokot G, Kebe TŠ, Žekš B, Waugh RE. A novel strain energy relationship for red blood cell membrane skeleton based on spectrin stiffness and its application to micropipette deformation. Biomech Model Mechanobiol. 2016; 15: 745–758.

119. Iglic A, Kralj-Iglic V, Hägerstrand H. Amphiphile induced echinocyte—spheroechinocyte red blood cell shape transformation. Eur Biophys J. 1998; 27: 335–339.

120. Iglic A, Svetina S, Zeks B. Depletion of membrane skeleton in red blood cell vesicles. Biophys J. 1995; 69: 274–279.

121. Spangler EJ, Harvey CW, Revalee JD, Kumar PBS, Laradji M. Computer simulation of cytoskeleton-induced blebbing in lipid membranes. Phys Rev E Stat Nonlin Soft Matter Phys. 2011; 84: 051906.

122. Hägerstrand H, Kralj-Iglic V, Bobrowska-Hägerstrand M, Iglic A. Membrane skeleton detachment in spherical and cylindrical microexovesicles. Bull Math Biol. 1999; 61: 1019–1030.

123. Goujon A, Colom A, Straková K, Mercier V, Mahecic D, Manley S, et al. Mechanosensitive Fluorescent Probes to Image Membrane Tension in Mitochondria, Endoplasmic Reticulum, and Lysosomes. J Am Chem Soc. 2019; 141: 3380–3384.

124. Vasan R, Maleckar MM, Williams CD, Rangamani P. DLITE Uses Cell-Cell Interface Movement to Better Infer Cell-Cell Tensions. Biophys J. 2019; 117: 1714–1727.